



2 Impact of penetrative solar radiation on the diagnosis of water mass 3 transformation in the Mediterranean Sea

4 Alexandra Bozec,^{1,3} Pascale Bouruet-Aubertot,¹ Daniele Iudicone,² and Michel Crépon¹

5 Received 23 October 2007; revised 24 January 2008; accepted 13 February 2008; published XX Month 2008.

6 [1] We applied a revised diagnosis of water mass formation and mixing to a 1/8°
7 resolution ocean model of the Mediterranean Sea. The diagnosis method used and
8 presented by Iudicone et al. (2007) is similar to that developed by Walin (1982) and
9 applied to the Mediterranean Sea by Tziperman and Speer (1994), to which we added a
10 penetrative solar radiation. Both the prognostic model and the diagnostic method
11 were in agreement with respect to the solar flux parameterization. Major changes were
12 observed in the yearly budget of water mass transformation when the penetrative
13 solar radiation is taken into account in the diagnosis. Annual estimates of water mass
14 formation rates were decreased by a factor of two, with values within the range
15 [−3.7 Sv, 1.5 Sv] compared to [−6 Sv, 3 Sv]. This decrease resulted from a lower seasonal
16 variation when penetrative solar radiation was included. This can be explained by the
17 fact that the solar radiation flux acted over a wider range of seawater density leading to
18 lower net values over a given density interval. The major impact of the penetrative solar
19 radiation occurred during spring and summer. Newly formed dense water was then
20 transformed into lighter water with a rate reaching a value about 50% of that of the water
21 mass formation rate in winter. Another consequence was that mixing processes which
22 counteract formation rate in yearly budget of water mass formation rates, were
23 overestimated. We showed that, in spring and summer, about a third of the transformation
24 took place below the surface layer.

25 **Citation:** Bozec, A., P. Bouruet-Aubertot, D. Iudicone, and M. Crépon (2008), Impact of penetrative solar radiation on the diagnosis
26 of water mass transformation in the Mediterranean Sea, *J. Geophys. Res.*, 113, XXXXXX, doi:10.1029/2007JC004606.

28 1. Introduction

29 [2] Solar radiation is one of the main forcing factors that
30 drive the ocean circulation, through the creation of horizon-
31 tal density gradients and water mass formation. How this
32 solar radiation is absorbed in the first hundred meters of the
33 ocean basically depends on the pigments and particle
34 concentration of the seawater [Jerlov, 1968; Morel and
35 Antoine, 1994; Frouin and Jacobellis, 2002]. This penetra-
36 tive radiation is of particular importance in regions with a
37 shallow mixed layer, such as tropical regions, as evidenced
38 by Lewis et al. [1990] and later by Murtugudde et al.
39 [2002]. In particular, Lewis et al. [1990] showed that the
40 introduction of a penetrative solar radiation into models
41 greatly improved the estimate of the sea-surface temperature
42 in the tropical Pacific Ocean. This results from the fact that
43 a nonnegligible amount of the net heat flux is absorbed
44 below the surface leading to a decrease in the sea surface

temperature with respect to the non penetrative solar case. 45
Also, this redistribution of heat into deep water could be of 46
primary importance in water mass transformation [Iudicone 47
et al., 2007]. For instance an overestimate of the ocean 48
surface heating could lead to an overestimate in water mass 49
transformation toward water of lower density. As a conse- 50
quence, the whole water mass transformation annual cycle 51
could be modified. Thus taking into account this penetration 52
of the solar radiation in the prognostic model, as well as in 53
the diagnosis of water mass formation, is of primary 54
importance. 55

[3] Water mass formation is classically diagnosed from 56
the surface heat flux, following the method introduced by 57
Walin [1982] and later extended by Tziperman [1986], who 58
also considered freshwater flux. This approach based on 59
surface fluxes provides an estimated upper boundary for 60
water mass formation which can be significantly reduced by 61
diffusion processes in the upper ocean [e.g., Tziperman, 62
1986]. Hence Marshall et al. [1993] later introduced a 63
refined diagnosis which allows the computation of subduc- 64
tion rates across a control surface below the mixed layer. 65
The penetration of solar radiation into the ocean subsurface 66
water was not taken into account in these calculations. The 67
inclusion of this penetration factor in the diagnosis has been 68
achieved only recently, by Iudicone et al. [2007] who 69
studied its impact in the tropics and in the Southern Ocean 70
using an ocean general circulation model (OGCM). They 71

¹Laboratoire d'Océanographie et de Climatologie - Expérimentation et Applications Numériques, LOCEAN/IPSL (previously LODYC), Paris, France.

²Laboratory of Biological Oceanography, Stazione Zoologica, SZN, Naples, Italy.

³Now at COAPS, Florida State University, Tallahassee, Florida, USA.

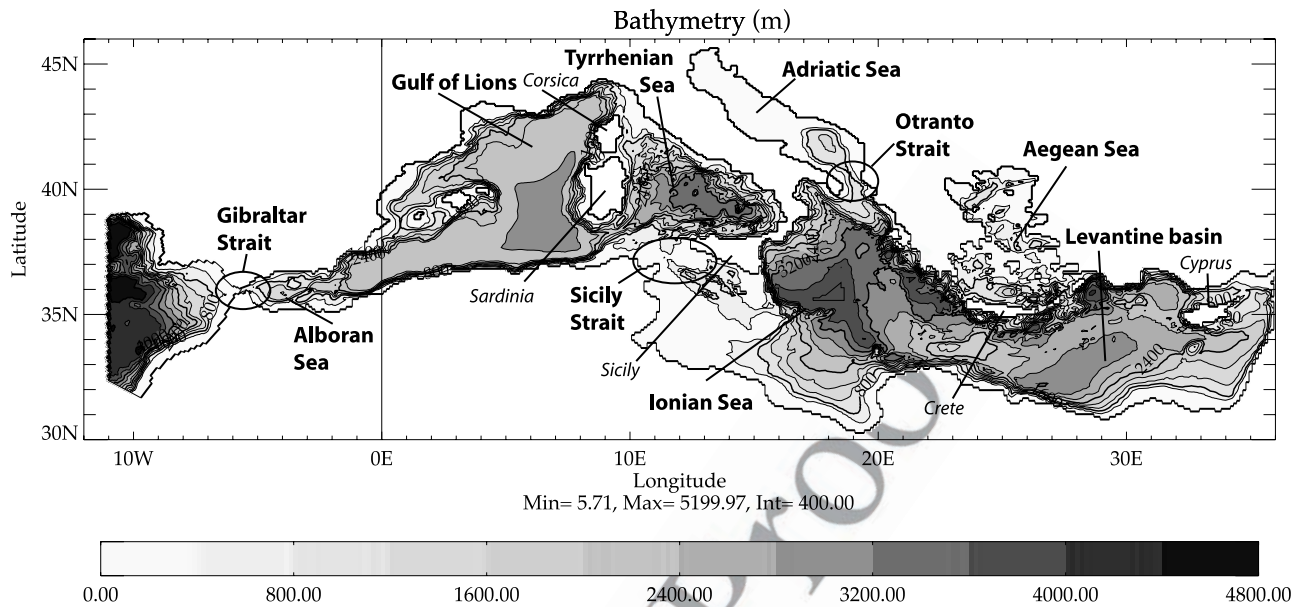


Figure 1. Bathymetry of the MED8 model, with isobath intervals of 400 m. The main locations cited in the text are also displayed on the figure.

72 found that at global scale the classical method overestimates
73 the seasonal cycle of the water masses transformation by a
74 factor close to 100%.

75 [4] The purpose of our study was to present revised
76 estimates of Mediterranean water mass formation and mixing
77 and to determine the effect of the penetrative solar radiation
78 on the diagnosis of water mass formation in the
79 Mediterranean Sea, using the output of an ocean model
80 including this parameterization. In this context, the choice
81 of the Mediterranean Sea was particularly relevant, since
82 this semi-enclosed sea has its own specific thermohaline
83 circulation [Wust, 1961; Lacombe and Tchernia, 1972;
84 Lascaratos et al., 1999]. This thermohaline circulation can
85 be thought of as a progressive transformation of the Atlantic
86 surface inflow, under atmospheric forcing into intermediate
87 and deep water. This transformation occurs in a few
88 locations and feeds the Mediterranean outflow through the
89 Strait of Gibraltar. The yearly transformation cycle has been
90 estimated by Tziperman and Speer [1994], who applied the
91 Walin [1982] and Tziperman [1986] methods to climatological
92 data. They found that the surface heat flux is mainly
93 responsible for the formation of water of maximal and
94 minimal density and for the destruction of water of intermediate
95 density, with annual formation rates in the range $[-4 \text{ Sv},$
96 $2 \text{ Sv}]$. Water mass transformation is counterbalanced by
97 mixing.

98 [5] The present work was to provide a refined diagnosis
99 of water mass formation rates in the Mediterranean Sea,
100 based on the analysis of numerical simulations of the whole
101 Mediterranean Sea. To do so, we introduced a parameterization
102 of the penetrating solar radiation into the Tziperman
103 and Speer diagnostics. Besides, we quantified the influence
104 of the introduction of a penetrative solar radiation flux into
105 this diagnosis and we established water mass budgets in the
106 mixed layer of the ocean and below the mixed layer.

107 [6] This paper is organized as follows. In section 2, we
108 describe the oceanic numerical model used in our study.

Section 3 covers the description of the atmospheric forcing 109
and a validation of the simulation. Section 4 covers: the 110
revised method for the diagnosis of water mass transforma- 111
tion, as well as a comparison with the “classical” diagnosis 112
[e.g., Tziperman and Speer, 1994]; the revised estimation of 113
the mixing of water masses and the annual and the seasonal 114
budgets during spring and summer, when the impact of the 115
penetrative solar radiation is maximal; and a detailed budget 116
of the water masses in the mixed layer and below it. Results 117
are discussed in section 5 (Conclusions). 118

2. Model Description 119

[7] The numerical model, hereafter referred to as MED8, 120
encompasses all the Mediterranean basin and has a resolu- 121
tion of $1/8^\circ$ for longitude and $1/8^\circ \cos\phi$ for latitude. MED8 122
is one of the Mediterranean configurations of the oceanic 123
model OPA [Madec et al., 1998]. This configuration was 124
derived from the MED16 configuration of the French 125
MERCATOR project [Drillet et al., 2000; Siefridt et al., 126
2002; Béranger et al., 2004]. The model domain extends 127
from 29°N to 46°N latitude and from 12°W to 38°E 128
longitude, thus including part of the Atlantic Ocean (Gulf 129
of Cadiz; Figure 1). The latter region was modeled as a 130
buffer zone, with a decreasing 3-D relaxation to the MED- 131
ATLAS II climatology [MEDAR/MEDATLAS Group, 2002] 132
from the western boundary to Gibraltar. Partial step for 133
bathymetric modeling has been implemented [Pacanowski 134
and Gnanadesikan, 1998], which greatly improves the 135
representation of the circulation. The vertical grid has 43 136
levels with vertical spacing varying from 6 m at the sea 137
surface down to a depth of 200 m. Viscosity and diffusive 138
terms were modeled with a bi-Laplacian in the horizontal 139
with diffusivity and viscosity coefficients equal to $-2.5 \times$ 140
 $10^{10} \text{ m}^4 \text{ s}^{-1}$. 141

[8] Vertical eddy diffusivity and viscosity were computed 142
from a level 1.5 turbulent closure scheme [Blanke and 143

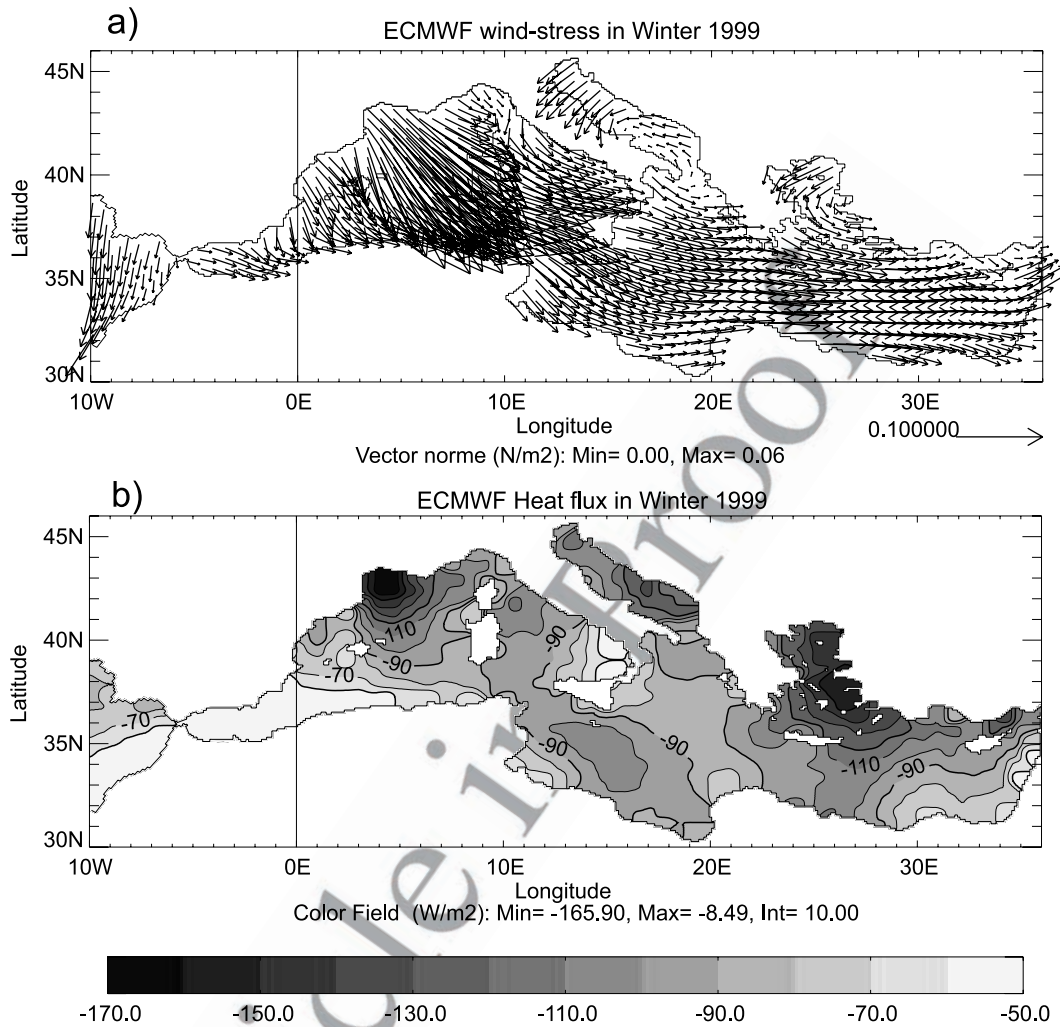


Figure 2. ECMWF atmospheric forcing averaged over winter 1999: (a) the wind stress (in N m^{-2}) is represented by *arrows*, (b) heat flux in W m^{-2} ; positive values indicate heat flux from the atmosphere to the ocean.

144 *Delecluse*, 1993], with a background value of $1 \times 10^{-5} \text{ m}^2 \text{ s}^{-1}$
 145 for both vertical viscosity and diffusivity. A “Monotonic
 146 Upstream-centered Scheme for Conservation Laws” was
 147 used as an advection scheme for tracers [*Lévy et al.*, 2001].
 148 Note that simulations were performed within the rigid-lid
 149 approximation. The initial temperature and salinity fields
 150 were derived from the MEDATLAS II monthly climatology
 151 [*MEDAR/MEDATLAS Group*, 2002]. Wind stress data and
 152 air–sea fluxes were obtained from the European Centre
 153 for Medium Range Weather Forecasting (ECMWF).
 154 Solar radiation flux is a function of depth, as described in
 155 section 4.1.1. Heat flux was applied at the model surface
 156 using the correction method [*Barnier et al.*, 1995], which
 157 combines a climatological record of the atmospheric heat
 158 flux and a retroaction term modeled as a relaxation term. In
 159 our study, this term includes a variable relaxation coefficient
 160 ranging from $-10 \text{ W m}^{-2} \text{ K}^{-1}$ in winter to $-40 \text{ W m}^{-2} \text{ K}^{-1}$
 161 in summer and relaxes the modeled SST toward the SST of
 162 *Reynolds* [1988]. The resulting heat flux is referred to as the
 163 net heat flux. Freshwater fluxes (evaporation, precipitation
 164 and river runoffs) were applied as a virtual salt flux that
 165 includes a relaxation term equivalent to $-40 \text{ W m}^{-2} \text{ K}^{-1}$,

constant over the year. A UNESCO monthly climatology 166
 of 31 river runoffs based on the RivDis database was 167
 implemented including the Black Sea outflow to the 168
 Aegean Sea. 169

3. Validation of the Simulation 170

3.1. ECMWF Atmospheric Forcing 171

[9] A specific feature of the atmospheric circulation over 172
 the Mediterranean Sea, due to the complex orography, is the 173
 presence of local winds, such as the Mistral [Gulf of Lions; 174
Madec et al., 1996] or the Etesian wind (Aegean Sea). The 175
 result is that only high-resolution atmospheric models are 176
 able to reproduce these local features [*Horton et al.*, 1994]. 177
 We considered here the high-resolution ECMWF analysis 178
 (equivalent to $0.5^\circ \times 0.5^\circ$) which allows a good represen- 179
 tation of local winds over the period 1998–2002. An 180
 example of these local winds is shown in Figure 2 where 181
 the winter average of the wind stress field is displayed. In 182
 the western basin, the strong local wind blowing southeast- 183
 ward, called the Mistral, contributes to deep water formation 184
 [*MEDOC Group*, 1970; *Madec et al.*, 1996]. This wind is 185

t1.1 **Table 1.** Yearly Averaged Heat Flux and Equivalent Freshwater Flux for the Whole Mediterranean Basin^a

t1.2	Heat Flux, W m^{-2}	E-P-R Flux, mm d^{-1}
t1.3	ECMWF-atmosphere -28.3 ± 123.4	1.67 ± 1.02
t1.4	ECMWF-ocean -2.79 ± 130.9	0.64 ± 1.22

t1.5 ^aECMWF-ocean includes the atmospheric forcing provided by the atmospheric ECMWF model plus the river run-off (ECMWF-atmosphere) and the restoration term for the heat flux or the relaxation term for the equivalent freshwater flux.

186 well represented in the high-resolution model (Figure 2a). In
187 the eastern basin, the cold and dry Etesian wind plays a
188 major role. Its cyclonic circulation, blowing from the
189 northeast, north of the Aegean Sea, and then from the
190 northwest in the Levantine basin, is present in the ECMWF
191 output.

192 [10] Statistics of the total heat flux and freshwater budget
193 are given in Table 1. The sign convention for heat flux is
194 positive from the atmosphere to the ocean. Note that both
195 intrinsic and real values, i.e., including the restoring term,
196 are displayed. In the model, the yearly mean surface heat
197 flux (atmospheric flux plus retroaction term) was -2.79 W
198 m^{-2} . This is consistent with observations [Béthoux, 1979;
199 MacDonal et al., 1994] that indicate a heat loss from the
200 Mediterranean Sea to the atmosphere between 3 and 7 W
201 m^{-2} (heat advected through the Strait of Gibraltar ensures
202 conservation of heat). Similarly, the equivalent freshwater
203 flux at the atmosphere–ocean interface (evaporation minus
204 precipitation minus runoff) is underestimated by the model.
205 The average model value of 0.64 mm d^{-1} over the Medi-
206 terranean basin, is significantly smaller than the 2.5 mm d^{-1}
207 inferred from observations [Garrett et al., 1993].

208 [11] To get a deeper understanding of the spatial distri-
209 bution of the total heat flux during the key wintertime
210 period, a map is given in Figure 2b. Higher values for the
211 heat loss were obtained in the main regions of convection,
212 namely in the Levantine basin, in the Adriatic Sea and in the
213 Aegean Sea for the eastern basin, as described by Lascaratos
214 et al. [1999], and in the Gulf of Lions for the western basin
215 [MEDOC Group, 1970]. These values were in agreement
216 with observations: $\sim -100 \text{ W m}^{-2}$ in the Adriatic Sea
217 [Artegiani et al., 1997]; and $\sim -110 \text{ W m}^{-2}$ in the Gulf of
218 Lions [Mertens and Schott, 1998], which was of particular
219 relevance for our simulations, since a high heat loss is
220 necessary to drive the preconditioning phase of the convec-
221 tion [e.g., Schott and Leaman, 1991, for the Gulf of Lions].

222 3.2. Oceanic Circulation

223 [12] The oceanic model was forced during 12 years with
224 three cycles of the four years (1998–2002) of the high-
225 resolution atmospheric model (ECMWF). The kinetic ener-
226 gy reached a steady state after 8 years. These first 8 years
227 were considered as the spin-up of the model. The initial
228 state was inferred from the MEDATLAS II climatology
229 [MEDAR/MEDATLAS Group, 2002]. The simulation was
230 started in August, when the surface layer is strongly
231 stratified, and the atmospheric forcing is weak. This ensures
232 that the effects of mixing were weak at the beginning of the
233 spin-up period. A brief description of the oceanic circulation
234 is given in the following subsections. The main purpose is

to show the ability of the model to reproduce intermediate 235
and deep water formation. 236

3.2.1. Surface Currents 237

[13] The surface current field is shown in Figure 3a. In 238
the western basin, the Atlantic inflow first forms the anti- 239
cyclonic Alboran gyre, east of the Strait of Gibraltar, as 240
described by Vargas-Yañez et al. [2000]. Then, this inflow 241
flows eastward along the North African coast forming the 242
Algerian Current. In the Tyrrhenian Sea, between Sardinia 243
and Italy, the Atlantic water, now called Modified Atlantic 244
Water (MAW), splits into two branches: the first one flows 245
through the Strait of Sicily and enters the eastern basin, 246
while the second one flows north of Sicily into the Tyr- 247
rhenian Sea [Astraldi et al., 2002]. This latter branch then 248
moves along the Italian coast to the French coast and feeds 249
the “Liguro-Provençal” Current, in agreement with Millot 250
[1999]. 251

[14] In the Strait of Sicily, the eastward branch of the 252
MAW separates into two branches as it enters the Ionian 253
Sea, as shown by Béranger et al. [2004]. One of these 254
branches follows the North African coast, while the other 255
one follows a more sinuous path in the northern part of the 256
Ionian Sea, becoming the Atlantic–Ionian Stream [Robinson 257
et al., 1999]. In the Southern Adriatic Sea, surface water 258
originating in the eastern basin flows through the Strait of 259
Otranto and mixes with the Adriatic water in the cyclonic 260
gyre in the southern part of the basin [Poulain, 2001]. In the 261
Levantine basin, the cyclonic circulation along the Middle- 262
East coast is in agreement with that described by Alhammoud 263
et al. [2005]. 264

3.2.2. Mixed-Layer Depth 265

[15] A snapshot of the maximum mixed-layer depth in 266
February is given in Figure 3b. The mixed-layer depth is 267
defined as the depth at which the potential density exceeds 268
the surface value by 0.01 kg m^{-3} . This parameter is a good 269
indicator of the ability of the model to represent the 270
formation of intermediate and deep waters. 271

[16] Four main sites of water mass formation were thus 272
identified: the Gulf of Lions, in the western basin; the 273
Adriatic Sea; the Levantine basin; and the Aegean Sea, in 274
the eastern basin. In the model, the mixed-layer depth has a 275
significant interannual variation. In the Gulf of Lions, 276
mixed-layer depth varied from 800 to 2700 m during the 277
simulation (Figure 3b). In the Levantine basin, intermediate 278
water was formed at a depth between 400 and 500 m. In the 279
Adriatic Sea, the mixed-layer often went below 900 m, 280
down to 1100 m at the end of the simulation. Finally, in the 281
western part of the Cretan Sea, some Cretan Intermediate 282
Water was formed, with a mixed-layer depth of 800 m 283
(Figure 3b). 284

[17] These results compared quite well with observations. 285
The mixed-layer depth in the Gulf of Lions, where the 286
Western Mediterranean Deep Water (WMDW, potential 287
density $\rho > 29.05 \text{ kg m}^{-3}$) forms, can reach 2700 m (bottom 288
of the basin) with a significant interannual variation 289
[MEDOC Group, 1970]. At intermediate depth, Western 290
Intermediate Water (WIW) also forms, between 150 and 291
250 m, with a potential density greater than 28.8 kg m^{-3} 292
[Fuda et al., 2000]. In the eastern basin, the mixed-layer 293
depth can exceed 1000 m in the Adriatic Sea, where the 294
Eastern Mediterranean Deep Water (EMDW) is formed, 295
with potential density greater than 29.1 kg m^{-3} [Roether 296

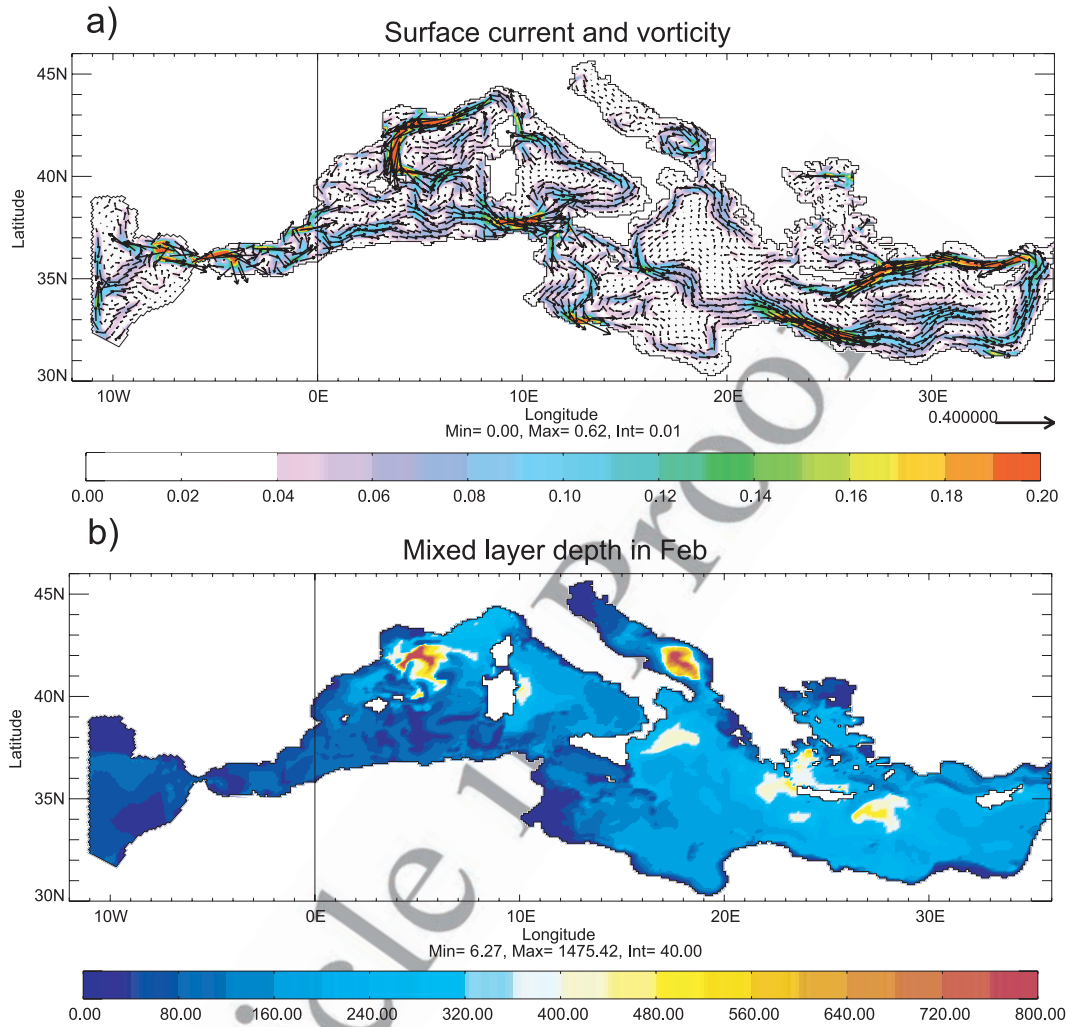


Figure 3. (a) Mean surface circulation in winter: the relative vorticity (s^{-1}) is represented by a *color-scale* and the current (m s^{-1}) is indicated by the *arrows*. (b) Snapshot of maximum mixed-layer depth (m) in February of year 10.

297 and Schlitzer, 1991; Vilibic and Orlic, 2002]. In the Levantine Basin, the mixed-layer depth can reach about 500 m
 298 where Levantine Intermediate Water (LIW) was formed
 299 ($28.9 < \rho < 29.1 \text{ kg m}^{-3}$ [Roether et al., 1998]). This depth
 300 can exceed 1000 m when Levantine Deep Water is formed
 301 [Gertman et al., 1994]. In the Aegean Sea, Cretan Inter-
 302 mediate Water and Cretan Deep Water (above 2500 m) forms
 303 intermittently created, as described by Theocharis et al.
 304 [2002].
 305

307 4. Water Mass Formation

308 4.1. Revised Tziperman-Speer Method

309 [18] Since the prognostic model MED8 includes the
 310 penetration of the solar radiation, our revised diagnosis
 311 takes into account this parameterization.

312 4.1.1. Penetrative Solar Radiation

313 [19] The vertical penetration of the solar radiation is
 314 classically described by decreasing exponential functions
 315 versus depth. This decrease obviously depends on the
 316 characteristics of the water, mainly the concentration of
 317 pigments and particles in suspension [Morel and Antoine,

1994; Frouin and Iacobellis, 2002]. In the numerical model 318
 MED8, this effect is taken into account by using a depth 319
 dependency of the solar radiation flux given by the follow- 320
 ing equation (see Figure 4) which approximately models the 321
 spectral dependence of the attenuation on depth: 322

$$Q_{sol}(x, y, z) = Q_0(x, y) \left[\text{Re}^{-\frac{z}{\xi_1}} + (1 - R)e^{-\frac{z}{\xi_2}} \right] \quad (1)$$

Where $Q_0(x, y)$ is the solar radiation flux across the sea 324
 surface at each point. The parameters $\xi_1 = 0.35 \text{ m}$, $\xi_2 = 23 \text{ m}$ 325
 and $R = 0.58$ correspond to a Type I water in the classification 326
 of Jerlov [1968]. 327

[20] Prior to a detailed analysis, it is useful to get a first 328
 insight into the impact of the penetrative solar radiation on 329
 water mass formation, in the MED8 model. This impact 330
 depends on the stratification of the upper layer which 331
 determines the density range of the seawater influenced 332
 by the penetrative solar radiation. This effect is clearly 333
 evident when the vertical profiles of the seasonally averaged 334
 potential density (reference in surface) and that of the solar 335
 heat flux are compared (Figure 4a). Note that each season 336

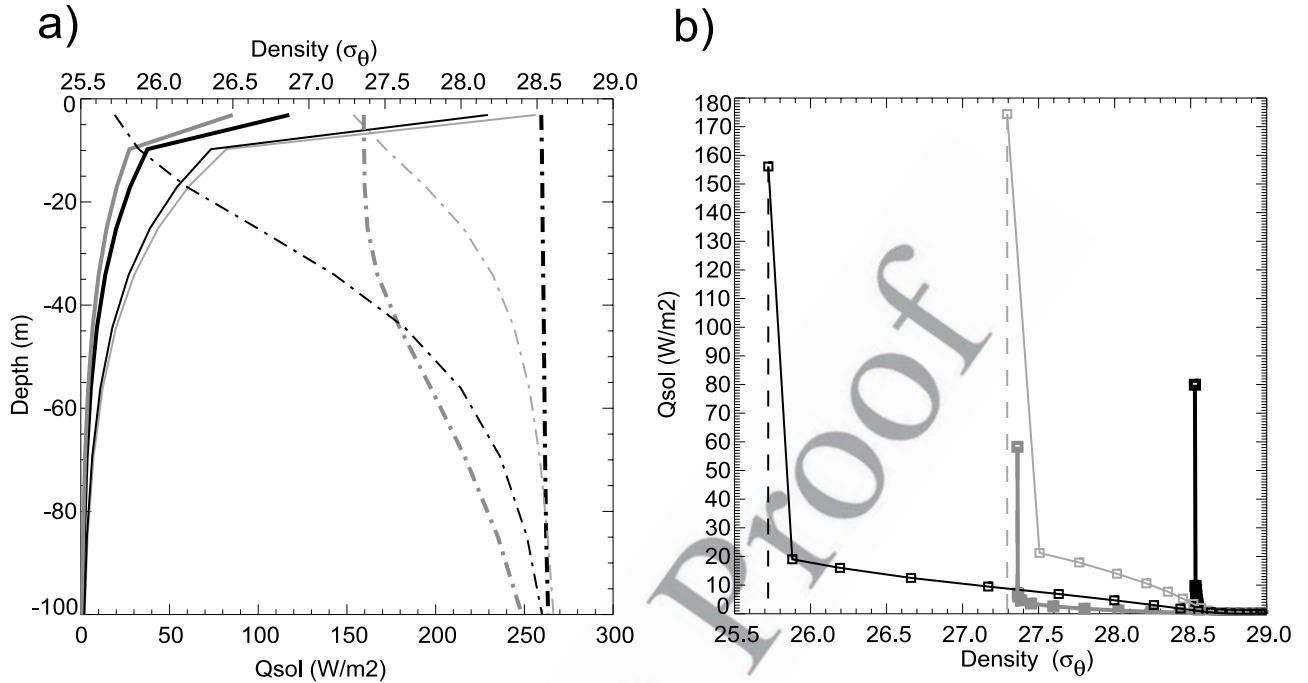


Figure 4. (a) Mean seasonal potential density profiles (in kg m^{-3} ; dash-dotted lines) and penetrative solar radiation (Q_{sol} in W m^{-2} ; full lines) versus depth for the whole Mediterranean Sea. Each season is color-coded so that winter (January–February–March) corresponds to the thick black line, autumn to the thick grey line, summer to the thin black line, spring to the thin light-grey line; (b) Penetrative solar radiation versus mean seasonal potential density, with the same color-code as in Figure 4a.

337 corresponds to three full months: winter is January, Febru-
 338 ary, March; spring is April, May, June; summer is July,
 339 August, September; and autumn is October, November,
 340 December. One can easily see that the widest density range
 341 corresponds to the solar heat flux in spring and summer. The
 342 strongest density variations occurred during these two
 343 seasons in the first 60 m of the water column, for which
 344 the solar heat flux was significant (160 W m^{-2} at the surface
 345 to 5 W m^{-2} at 60 m depth, in summer, and 170 W m^{-2} at
 346 the surface to 5 W m^{-2} at 60 m depth, in spring). For a
 347 quantitative characterization of this effect, the solar heat
 348 flux received per density range averaged over the Mediter-
 349 ranean basin is given in Figure 4b, for the four seasons. The
 350 range of potential density influenced by the solar radiation
 351 is 2.8 kg m^{-3} , in summer, and 1.2 kg m^{-3} , in spring,
 352 whereas this range tends to zero in autumn and winter,
 353 owing to the almost insignificant stratification in the first
 354 60 m due to mixing.

4.1.2. The Revised Diagnosis Computation

356 [21] An upper limit for water mass formation can be
 357 derived from the buoyancy forcing. The method was
 358 developed by *Walsh* [1982] who computed the net volume
 359 flux per density interval from the surface heat flux. Later
 360 *Tziperman* [1986] included the surface water flux, while
 361 *Nurser et al.* [1999] and *Marshall et al.* [1993] added the
 362 diffusive diapycnal fluxes. Finally, a generalized approach
 363 was proposed by *Iudicone et al.* [2007] that includes the
 364 penetrative character of the solar radiative flux and the use
 365 of a neutral density framework. In the following we use the
 366 method presented by *Iudicone et al.* [2007]:

[22] The buoyancy flux per unit area, B_m , is computed as 367
 follows: 368

$$B_m = g \frac{\alpha}{C_p} Q_{\text{tot}} - g\beta S(E - P) \quad (2)$$

where $E - P$ is the net water flux (evaporation–precipitation– 370
 runoff (in $\text{kg m}^{-2} \text{ s}^{-1}$)) acting at the sea surface, S is the 371
 surface salinity, C_p the specific heat (equal to 4000 J kg^{-1} 372
 K^{-1}), $\alpha = -\frac{1}{\rho_0} \frac{\partial \rho}{\partial \theta}$ the thermal expansion coefficient and 373
 $\beta = \frac{1}{\rho_0} \frac{\partial \rho}{\partial S}$ the saline contraction coefficient. Q_{tot} is the total 374
 net heat flux into the ocean (in W m^{-2}). Q_{tot} is decomposed 375
 into a surface heat flux (longwave + latent + sensible heat 376
 flux + restoring) denoted Q_{nsol} and a heat flux acting in the 377
 mass of fluid, Q_{sol} . Thus Q_{tot} can be written as: 378

$$Q_{\text{tot}}(x, y, z) = Q_{\text{nsol}}(x, y) \delta_{z=0} + Q_{\text{sol}}(x, y, z) \quad (3)$$

where $\delta_{z=0}$ is the Dirac function equal to 1 at $z = 0$, and 0 380
 elsewhere. 381

[23] Since the prognostic model MED8 includes the 382
 penetration of the solar radiation, our revised diagnosis 383
 takes it into account. 384

[24] The mass transformation rate $\Phi(\rho)$ for a water of 385
 potential density ρ within $[\rho - \frac{1}{2}\Delta\rho, \rho + \frac{1}{2}\Delta\rho]$ is inferred 386
 from the buoyancy flux (equation (2)) integrated over a 387
 volume bounded by the density surfaces $\rho - \frac{1}{2}\Delta\rho$ and $\rho +$ 388
 $\frac{1}{2}\Delta\rho$ and over a duration T (Figure 5). It is driven first by 389
 surface effects due to Q_{nsol} and $E - P$ acting on the area A 390
 bounded by the outcropping density surfaces $\rho - \frac{1}{2}\Delta\rho$ and 391
 $\rho + \frac{1}{2}\Delta\rho$ and secondly by volume effects due to Q_{sol} acting 392
 on a volume V bounded by the density surfaces $\rho - \frac{1}{2}\Delta\rho$ and 393
 $\rho + \frac{1}{2}\Delta\rho$ (see Figure 5). The expression of the transformation 394

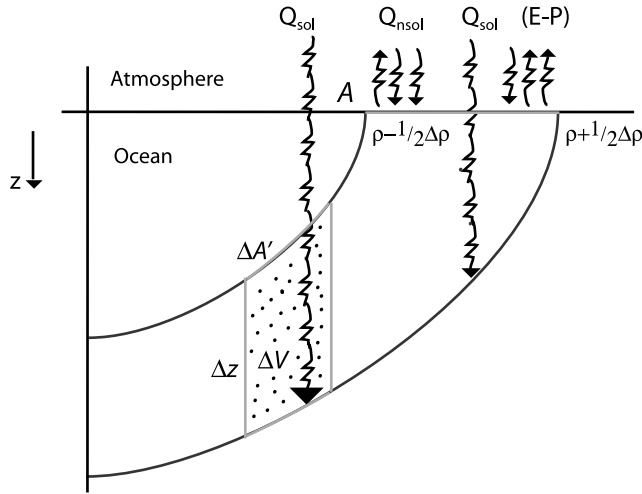


Figure 5. Scheme of the surface forcing effects on a density layer (dotted area) between $\rho - \frac{1}{2}\Delta\rho$ and $\rho + \frac{1}{2}\Delta\rho$. Q_{nsol} is the nonsolar heat flux, $E - P$ is the freshwater flux and Q_{sol} is the penetrative solar radiation.

395 rate is given by the following equation (Π corresponding to
396 the top-hat function equal to 1 for $\rho - \frac{1}{2}\Delta\rho < \rho < \rho + \frac{1}{2}\Delta\rho$, and
397 zero elsewhere):

$$\begin{aligned} \Phi(\rho) = & \frac{1}{T} \int_0^T dt \iint_A \left[\frac{\alpha}{C_p} Q_{nsol} - \beta S(E - P) \right] \\ & \cdot \Pi \left(\rho - \frac{1}{2}\Delta\rho, \rho + \frac{1}{2}\Delta\rho \right) dA \\ & + \frac{1}{T} \int_0^T dt \iint_{A'} \frac{\alpha}{C_p} \int_z \frac{\partial Q_{sol}(x, y, z)}{\partial z} \\ & \cdot \Pi \left(\rho - \frac{1}{2}\Delta\rho, \rho + \frac{1}{2}\Delta\rho \right) dz dA' \end{aligned} \quad (4)$$

399 As in the work of *Tziperman and Speer* [1994] let us
400 defined a volume transformation rate per density interval as
401 $F(\rho) = \lim(\Delta\rho \rightarrow 0) \frac{\Phi(\rho)}{\Delta\rho}$. The quantity F that is expressed in
402 Sv ($1 \text{ Sv} = 10^6 \text{ m}^3 \text{ s}^{-1}$), is a more familiar quantity than the
403 transformation rate Φ . Note that the difference with previous
404 methods consists in the inclusion of the solar irradiance as a
405 3-D term in (4).

406 [25] Equation (4) is discretized on the grid of the numer-
407 ical model, with volume grid cells $\Delta x \times \Delta y \times \Delta z$, with an
408 elementary density interval of width $\Delta\rho$ and for a duration
409 of $N\Delta t$. Only the term that includes the solar radiation flux
410 is discretized on the 3-D grid of the numerical model; the
411 others terms are only discretized on the horizontal grid. One
412 then gets the revised volume transformation rate per density
413 interval, F as:

$$\begin{aligned} F(\rho) = & \frac{1}{N\Delta t} \frac{1}{\Delta\rho} \sum_{n=1}^N \Delta t \sum_{ij} \Delta x \Delta y \left[\frac{\alpha}{C_p} Q_{nsol} - \beta S(E - P) \right] \\ & \cdot \Pi \left(\rho - \frac{1}{2}\Delta\rho, \rho + \frac{1}{2}\Delta\rho \right) \\ & + \frac{1}{N\Delta t} \frac{1}{\Delta\rho} \sum_{n=1}^N \Delta t \sum_{ijk} \Delta x \Delta y \Delta z \left[\frac{\alpha}{C_p} \frac{\partial Q_{sol}(x, y, z)}{\partial z} \right] \\ & \cdot \Pi \left(\rho - \frac{1}{2}\Delta\rho, \rho + \frac{1}{2}\Delta\rho \right) \end{aligned} \quad (5)$$

The quantity F corresponds to that defined by equation (4) 415
in the work of *Tziperman and Speer* [1994] with the same 416
sign convention (positive for a transformation from high to 417
low densities) to facilitate comparisons. 418

4.1.3. Impact of the Penetrative Solar Radiation in the Diagnosis of Water Mass Formation 419

[26] The purpose of this section is to provide a first 421
characterization of the impact of the penetrative solar 422
radiation in the diagnosis of water mass formation. For that, 423
as in the study by *Tziperman and Speer* [1994], we estimated 424
the annual volume transformation rate F (Figure 6a), 425
computed over the basin, using both the ‘‘classical’’ diag- 426
nosis and the ‘‘revised’’ diagnosis (equation (5)). For this 427
study, we chose a potential density increment $\Delta\rho = 0.12 \text{ kg}$ 428
 m^{-3} and a Δt of 1 month as by *Tziperman and Speer* 429
[1994]. We present here the analysis of year 10 of the 430
simulation, whose behavior is close to that of the other 431
years. The mean annual transformation rate per density 432
interval $\Delta\rho$ (i.e., $F(\rho)$ expressed in Sv) is shown in Figure 6. 433

[27] The annual transformation rate computed with the 434
classical method (grey line in Figures 6a, 6c, and 6e) is 435
similar in shape to that obtained by *Tziperman and Speer* 436
[1994, Figure 1] but their values are slightly lower than 437
ours, which can be attributed to the fact that they analyzed 438
climatological data and not model data as in this study. The 439
transformation rate presents a maximum at $\sigma_\theta = 26 \text{ kg m}^{-3}$ 440
corresponding to a flux of about 3 Sv flowing from greater 441
densities to lower ones. It is minimum at $\sigma_\theta = 28.7 \text{ kg m}^{-3}$, 442
corresponding to about 6 Sv of light waters transforming to 443
greater densities. Similarly, we found about 1 Sv of inter- 444
mediate and dense waters (WIW, LIW and WMDW) formed 445
in the western basin (Figure 6c) and 4.5 Sv (LIW and EMDW) 446
formed in the eastern Mediterranean basin (Figure 6e), as by 447
Tziperman and Speer [1994, Figures 2 and 3]. Finally, note 448
that from the analysis above, it results that, in the Mediter- 449
ranean Sea, the main part of the transformations takes place 450
in the eastern basin. 451

[28] The first striking effect of the use of a penetrative 452
solar radiation in the diagnosis is a reduction in the 453
amplitude of water mass transformation with an unchanged 454
shape. This is clearly seen in the yearly averaged transfor- 455
mation rates shown in Figures 6a, 6c, and 6e. The annual 456
cycle is significantly reduced when the penetrative solar 457
radiation is taken into account, with an amplitude of about 458
5.2 Sv, to be compared with the classical diagnosis range of 459
9 Sv for the whole Mediterranean Sea (Figure 6a). The most 460
important difference concerns the eastern basin, with a 461
range of 4.2 Sv in the seasonal cycle, to be compared to a 462
classical diagnosis range of 6.4 Sv. Transformation rates of 463
deep and intermediate waters change to a lesser extent, 464
except that of LIW which is decreased by about 20% 465
(Figures 6c and 6e). The impact of the new estimate 466
concerns mostly the MAW. The seasonally averaged trans- 467
formation rates are presented in Figures 6b, 6d, and 6f. 468

[29] As expected, the two methods provide almost identical 469
diagnoses in autumn and winter (Figures 6b, 6d, and 470
6f). This results from the fact that the mixed layer was 471
deeper than the penetration depth of the solar radiation, as 472
underlined in section 4.1.1. In contrast, major changes are 473
observed in spring and summer (Figures 6b, 6d, and 6f). 474
With the revised method, a larger density range is influ- 475
enced by the penetrative solar radiation due to the shallow- 476

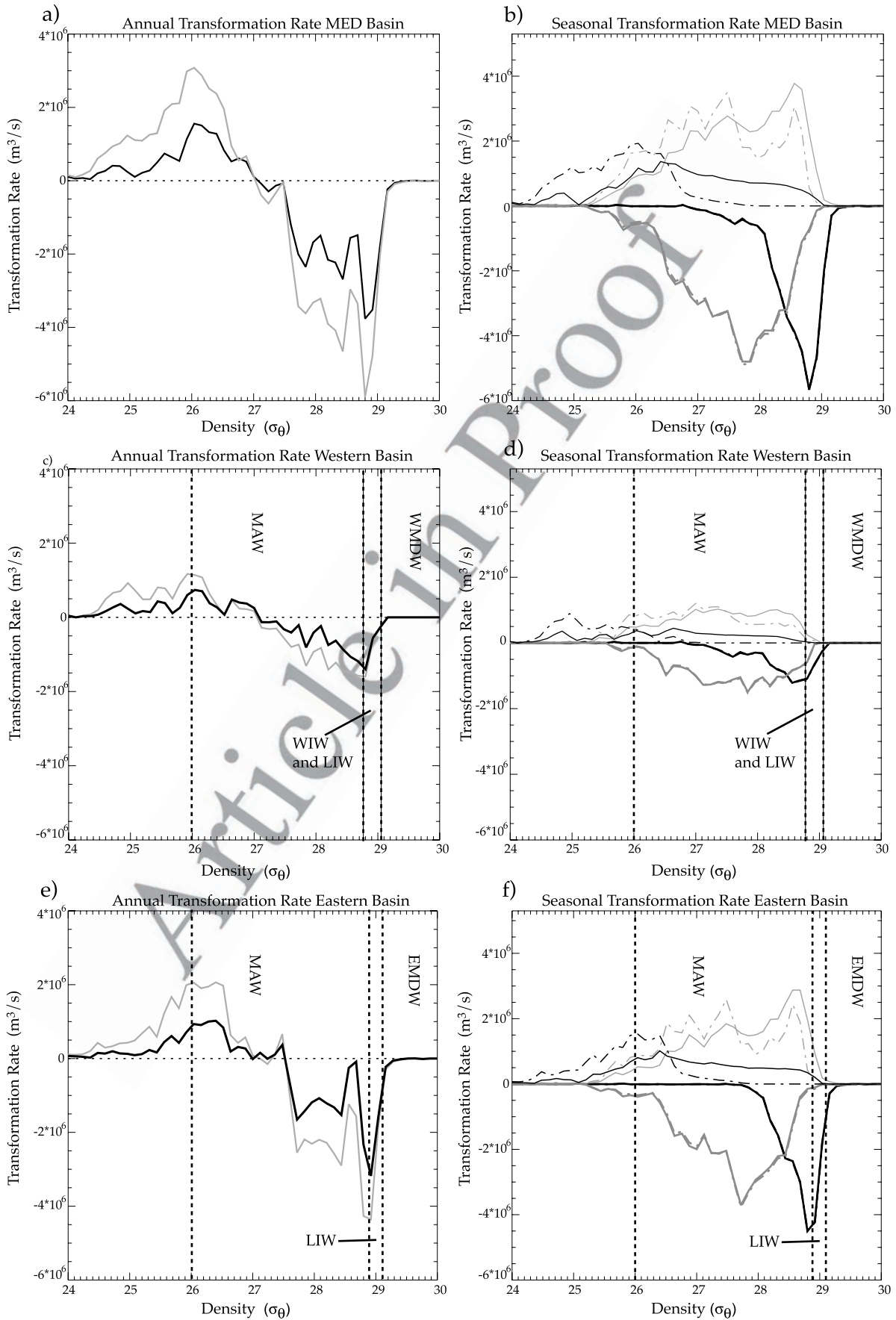


Figure 6

ness of the mixed layer. This has two main consequences. First a weaker transformation rate is obtained for the lowest densities, i.e., surface waters, due to a reduced solar heating contribution. Secondly, it highlights the contribution of the penetrative solar radiation to the transformation of fairly high-density water into lighter water, due to a reduced absorption of solar radiation in the mixed layer. More precisely, in spring the transformation rate is reduced for potential densities less than $\sigma_\theta = 27.6 \text{ kg m}^{-3}$ and increased for higher densities, up to 29 kg m^{-3} . Also, the upper boundary of the density range influenced by the solar radiation flux is slightly shifted, from 28.8 to 29 kg m^{-3} , during these seasons in the eastern basin, showing the partial destruction of the LIW formed in winter (Figure 6f). In the western basin, a more important quantity of WIW and LIW at densities between 28.6 and 29 kg m^{-3} (Figure 6d) is transformed into lighter water. The most important changes concerns the summer season when the solar radiation flux is maximum and the mixed layer at its shallowest. The density range influenced by the solar radiation flux is then much wider, reaching an upper boundary of 28.9 kg m^{-3} in the eastern basin (Figure 6f), to be compared to that of 27.5 kg m^{-3} obtained with the classical method and an upper boundary of 28.7 kg m^{-3} in the western basin (Figure 6) to be compared to that 26.8 kg m^{-3} with the classical method. These high-density waters (basically LIW) are then destroyed in summer. As a consequence of the reduced solar radiation flux with respect to the water of lowest density (surface water and MAW), their transformation rate is reduced. In summary, the main impact of the penetrative solar radiation is to destroy high-density water created during autumn and winter. The rate of destruction reaches 50% of the rate of formation (about 0.2 Sv in summer and about 1.1 Sv in spring; Figure 6b). This change is particularly relevant to the estimation of water mass mixing as discussed in the following. Indeed, using the classical method for determining water mass formation, the high-density water masses formed in autumn and winter were “seen” to be destroyed only through mixing, if one assumes zero annual variation in water volume in the Mediterranean Sea.

4.2. Revised Estimate of Mixing

[30] The analysis of the life cycle of water masses was conducted on the basis of volume budgets of water contained between two isopycnals. To this end we used the equation of conservation of water volume established by Nurser *et al.* [1999] [see also Large and Nurser, 2001],

which is valid under the Boussinesq approximation and for an incompressible fluid. The time derivative of a water volume of potential density ρ between the isopycnals $\rho - 1/2\Delta\rho$ and $\rho + 1/2\Delta\rho$ with open boundaries is given by:

$$\left(\frac{\partial\Delta V}{\partial t} + \Delta\psi\right) = \Gamma\left(\rho + \frac{1}{2}\Delta\rho\right) - \Gamma\left(\rho - \frac{1}{2}\Delta\rho\right) \quad (6)$$

where $\frac{\partial\Delta V}{\partial t}$ is the time variation in the volume between the isopycnals $\rho - 1/2\Delta\rho$ and $\rho + 1/2\Delta\rho$, $\Delta\psi$ is the volume flux of fluid (advective flux) exiting the domain, $\Gamma(\rho)$ a cross-isopycnal volume flux $\Gamma = F + \frac{\partial D_{diff}}{\partial\rho}$ in which $F(\rho)$ is the volume transformation rate from high to low densities computed from equation (5) and D_{diff} the diapycnal density flux, Volume variations resulting from mixing (i.e., D_{diff}) can thus be inferred indirectly from the volume budget (equation (6)). For the sake of simplicity, we analyzed the diapycnal transport across ρ , namely the volume budget for water lighter than ρ as deduced from the integration in ρ of equation (6). Let us now integrate equation (6) with respect to density intervals. We obtain a budget equation for density of the form:

$$\left(\overline{\frac{\partial\Delta V}{\partial t}} + \overline{\Delta\psi}\right) = \Gamma(\rho) \quad (7)$$

where $\overline{\frac{\partial\Delta V}{\partial t}}$ is equal to $\frac{1}{\rho - \rho_{min}} \int \frac{\partial\Delta V}{\partial t} d\rho$
 $\overline{\Delta\psi}$ is equal to $\frac{1}{\rho - \rho_{min}} \int \Delta\psi d\rho$

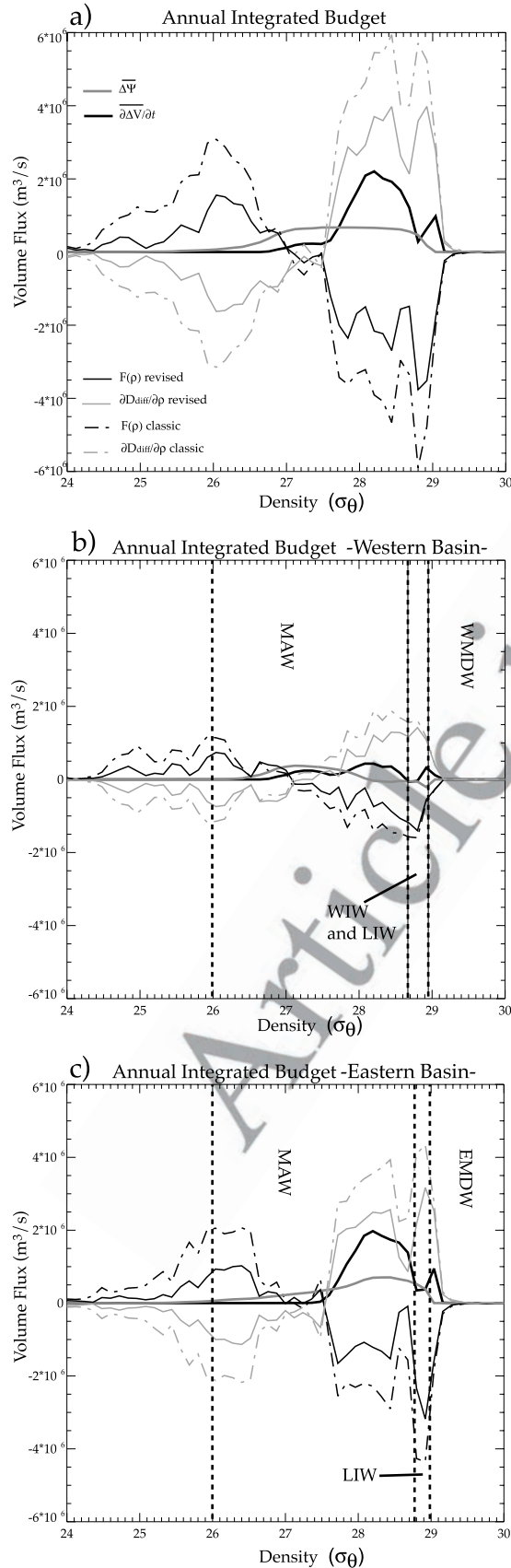
and ρ_{min} is the minimum density of the Mediterranean water under consideration.

4.2.1. Annual Water-Volume Budget

[31] The annual volume budgets per density interval integrated over the whole Mediterranean Sea (from equation (7)), are displayed in Figures 7a, 7b, and 7c. The budgets are computed for basins represented as boxes with open boundaries. For the Mediterranean Sea budget, the box includes the whole basin east of the Strait of Gibraltar (Figure 7a). For the western basin, the control volume occupies the part of the Mediterranean Sea lying between the Strait of Gibraltar and the Strait of Sicily (Figure 7b). Finally, the eastern basin is bounded by the Strait of Sicily (Figure 7c).

[32] These volume budgets revealed two predominant, mostly counteracting, terms: the transformation rate (in-

Figure 6. (a), (c), and (e): Annual water mass transformation rate ($F(\rho)$ in $\text{m}^3 \text{ s}^{-1}$ integrated over the whole density range versus density (kg m^{-3}), for year 10 of the simulation: for the whole Mediterranean basin (Figure 6a); for the western Mediterranean basin (Figure 6c); for the eastern Mediterranean basin (Figure 6e); the result for the classical method is represented by a *grey line* and for the revised method, by a *black line*. (b), (d) and (f): Seasonal transformation rate ($F(\rho)$, in $\text{m}^3 \text{ s}^{-1}$) integrated over the whole density range versus density (kg m^{-3}): for the whole Mediterranean basin (Figure 6b); for the western Mediterranean basin (Figure 6d); for the eastern Mediterranean basin (Figure 6f); the color-code for season is the following: winter in *thick black line*; spring in *thin light-grey line*; summer in *thin black line*; and autumn in *thick grey line*; the classical method is displayed by a *dashed line* and the revised method, with a *continuous line*. The potential density increment is $\Delta\rho = 0.12 \text{ kg m}^{-3}$. *Vertical dashed lines* bound the density intervals of the different water masses of the basin (for definition see section 3.2.2). *MAW* Modified Atlantic Water; *WMDW* Western Mediterranean Deep Water; *EMDW* Eastern Mediterranean Deep Water; *LIW* Levantine Intermediate Water; *WIW* Western Intermediate Water.



duced by atmospheric fluxes) and the diapycnal fluxes (i.e., 561
 mixing). The other terms are indeed much smaller, with an 562
 advective flux of about 0.75 Sv corresponding to the Strait 563
 of Gibraltar and a negligible volume variation, except for the 564
 highest-density water, with a value of about 2 Sv (Figure 7a). 565
 The transformation rate (i.e., $F(\rho)$) induced by the heat and 566
 freshwater flux is responsible for the formation of waters of 567
 minimal and maximal densities that were transformed by 568
 mixing into waters of intermediate densities. Conversely, 569
 these waters of intermediate densities were destroyed 570
 through heat and freshwater fluxes. Since the transformation 571
 rate is significantly overestimated by the classical method, 572
 revised estimates of diapycnal fluxes were significantly 573
 reduced, as shown in Figures 7a, 7b, and 7c. 574

[33] In the western basin, this overestimation of mixing 575
 mostly concerned the density range below $\sigma_\theta = 28.7$ kg 576
 m^{-3} . The transformation of MAW through mixing was 577
 overestimated by an amount of 1 Sv namely 30% of its 578
 previous value of 2.9 Sv and the volume of surface waters 579
 destroyed through mixing was overestimated by 0.5 Sv 580
 namely 42% of its previous value and that of the LIW and 581
 WIW by 0.5 Sv namely 30% its previous value (Figure 7b). 582
 In the eastern basin, transformation of MAW through 583
 mixing was overestimated by an amount of 2.2 Sv namely 584
 35% its previous value (Figure 7c). The diapycnal fluxes in 585
 the surface water density range were estimated at twice the 586
 revised value by the classical method (Figure 7c). In the 587
 LIW density range, the transformation rate and the diapycnal 588
 fluxes were also overestimated, by about 31% by the 589
 classical method. In the EMDW density range, we found 590
 similar values with the classical and the revised methods. 591

4.2.2. Seasonal Water-Volume Budget 592

[34] Seasonal integrated budgets are given in Figure 8. In 593
 autumn and winter the densest water is formed because of 594
 surface cooling and evaporation. The net volume variation 595
 (time derivative) of this newly formed water is slightly 596
 reduced by mixing (Figures 8c and 8d). During these two 597
 seasons, the transformation rate remained unchanged if the 598
 penetrative solar radiation was taken into account in the 599
 diagnosis, as previously mentioned. 600

[35] In spring the net variation in water volume was 601
 characterized by a decrease, for the densest water, of 602
 potential density greater than 28.4 kg m^{-3} , and by an 603
 increase, for the lightest water, of potential density between 604

Figure 7. Annual water volume budget versus potential density: (a) for the Mediterranean basin, (b) for the western basin, and (c) for the eastern basin. The different terms of equation (8) integrated over density are displayed: $\frac{\partial \Delta V}{\partial t}$, is represented by a *thick black line*, the advection term, $\Delta \psi$, by a *thick dark-grey line*, the diapycnal fluxes terms, $\frac{\partial D_{diff}}{\partial \rho}$, by a *thin light-grey line*, and the transformation rate (as in Figure 6), $F(\rho)$, by a *thin black line*. Terms inferred using the revised method are plotted with a *full line*, while those inferred using the classical method are plotted with a *dash-dotted line*. *Vertical dashed lines* mark the density layers of the different water masses of the basin (for definition see Figure 6 and section 3.2.2).

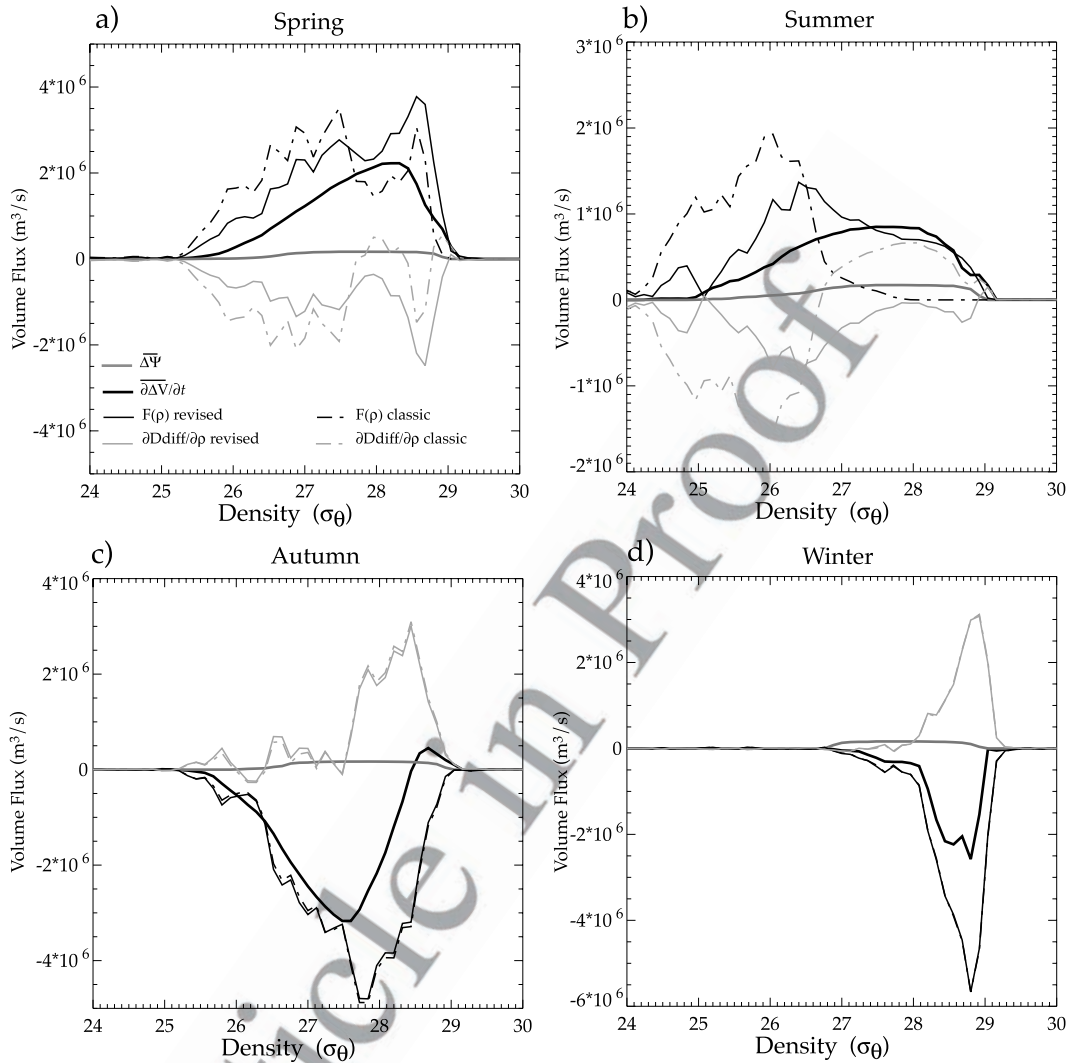


Figure 8. Seasonal water volume budget versus potential density: (a) in spring, (b) in summer, (c) in autumn, and (d) in winter; Color-coded lines as in Figure 7. Positive values of the slope are related to the formation of water masses, negative values, to the destruction of water masses.

605 25 and 28 kg m⁻³ (Figure 8a). Again both transformation
606 rate and diapycnal fluxes play a counteracting role in this
607 evolution, as detailed above.

608 [36] In the range $\sigma_\theta < 28$ kg m⁻³, the analysis of the
609 revised method showed an overestimation of the budget but
610 the shape of the different curves remains similar.

611 [37] The main difference appeared in the density range $\sigma_\theta =$
612 [28.6 kg m⁻³, 29.5 kg m⁻³], when taking into account the
613 penetrative solar radiation in the diagnosis: the transforma-
614 tion rate ($F(\rho)$) of the densest waters increased from 3 Sv with
615 the classical method to 4 Sv with the revised method and
616 covered a wider range (see section 4.1).

617 [38] As shown in section 4.1, in summer, the transforma-
618 tion rate computed with and without the penetrative solar
619 radiation method are strongly different, especially in the high
620 density range where a water mass formation can occur instead
621 of a destruction with the classical method (Figure 8b). In the
622 light density range, the volume budget is overestimated with
623 the classical method, as in spring. At densities greater than
624 $\sigma_\theta = 27$ kg m⁻³, the major effect of the penetrative solar

radiation was to transform dense water into lighter water. 625
Indeed, the transformation induced by heat and freshwater 626
flux estimated by the revised method accounts now for the 627
most important part of the destruction of waters of density 628
in the range $\sigma_\theta \geq 28$ kg m⁻³ with a rate of about 0.5 Sv 629
while the role of the diapycnal fluxes is strongly decreased 630
in this range. 631

4.3. Water Mass Budgets in the Surface Layers and in 632 the Ocean Interior 633

[39] The next step was to distinguish between water mass 634
transformation in the surface layers and in the ocean 635
interior. In this way we were able to provide a more accurate 636
estimate of the effective water mass formation, i.e., the 637
water-volume flux into the ocean interior. To this end, we 638
distinguish two control volumes: the first one is defined as 639
the volume of water in the surface layers and the second as 640
the water volume below. Since the only changes attributable 641
to the penetrative solar radiation occur in spring and 642
summer, we focused on these two seasonal budgets. In 643

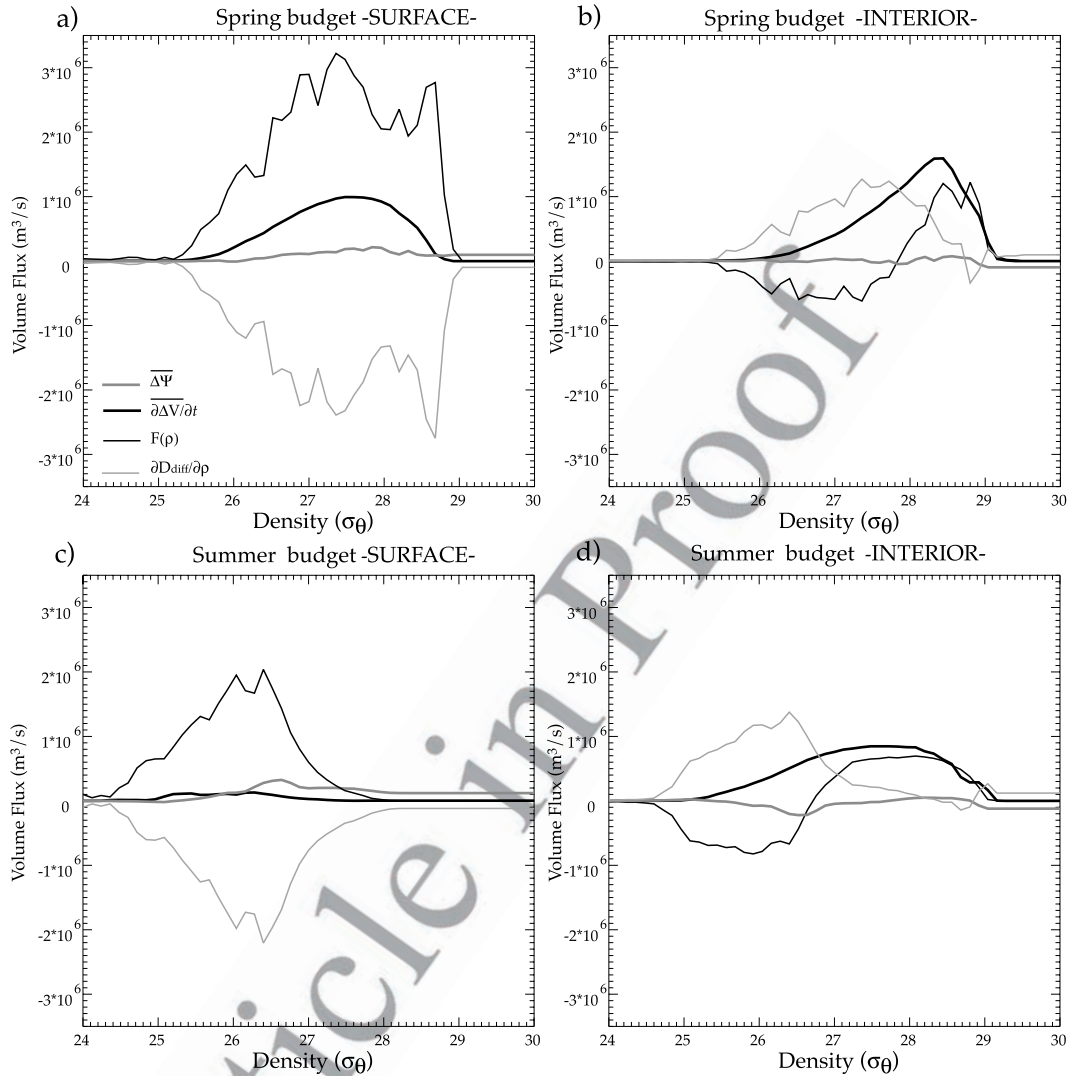


Figure 9. Seasonal water volume budgets versus potential density: (a) in spring for the surface layers (the maximum depth of this layer is equal to 17 m), (b) in spring for the ocean interior, (c) in summer for the surface layers (the maximum depth is equal to 9 m), and (d) in summer for the ocean interior; color-coded lines as in Figure 8. Positive values of the slope are related to the formation of water masses, negative values, to the destruction of water masses.

644 spring the surface layers are defined by the first 17 m of the
 645 ocean surface, corresponding to the first 3 vertical levels of
 646 MED8. In summer, these surface layers are set at 9 m,
 647 corresponding to the first 2 vertical levels. These surface
 648 layers roughly correspond to the mixed layer. Seasonal
 649 budgets for spring and summer in the surface layers and
 650 in the ocean interior are given in Figure 9. The budgets are
 651 averaged over the whole Mediterranean basin, as in the
 652 previous section, and are computed using the revised
 653 method only.

654 [40] The strongest volume variations occur in spring, with
 655 destruction of the densest water and creation of the lightest
 656 water. The transition between newly formed and destroyed
 657 water masses differs slightly between the surface layers and
 658 the ocean interior, with a potential density of 27.4 kg m^{-3} at
 659 the surface and a potential density of 28.4 kg m^{-3} in the
 660 interior (Figures 9a and 9b). The net volume flux reaches
 661 1.6 Sv in the interior (Figure 9b) and is about 1 Sv in the

surface layers (Figure 9a). The penetrative solar radiation 662
 plays a significant role in this evolution since, at depth, the 663
 volume transformation rate is induced only by this term. 664
 This factor is responsible for most of the transformation of 665
 the densest water, $\sigma_\theta > 28.7 \text{ kg m}^{-3}$, corresponding to about 666
 1 Sv (Figure 9b) into lighter water. It also plays an 667
 important role in the creation of water of intermediate 668
 density ($27.3\text{--}28.4 \text{ kg m}^{-3}$) corresponding to a value of 669
 nearly 2 Sv in the interior (Figure 9b). This strong trans- 670
 formation rate is, however, significantly counterbalanced by 671
 mixing, with the destruction of about 1 Sv of these waters, 672
 leading to a net formation of about 1 Sv in this density 673
 range. In contrast, mixing contributes mostly to the creation 674
 of the lowest-density water, while the penetrative solar 675
 radiation contributes to its destruction. 676

[41] In summer, most of the volume variations occur in 677
 the ocean interior. At the surface, the transformation rate 678
 and diapycnal fluxes terms are almost balanced. These two 679

680 terms play alternating roles, depending on the density range:
 681 water in the smaller density range were created by atmo-
 682 spheric fluxes and destroyed by mixing; and conversely,
 683 waters in the higher density range were created by mixing
 684 and destroyed by atmospheric fluxes. In the ocean interior, a
 685 similar pattern to that obtained in spring was observed. Thus
 686 the analysis reveals the important role of the penetrative
 687 solar radiation below the surface layers under the stratified
 688 conditions of spring and summer. Basically, this factor
 689 contributes to the destruction of the highest- and lowest-
 690 density water and to the creation of the intermediate-density
 691 water.

693 5. Conclusions

694 [42] In this work, we focused on the estimate of the
 695 impact of the penetrative solar radiation on the determina-
 696 tion of water mass transformation in the Mediterranean Sea.
 697 Water mass transformation is a key process that drives the
 698 Mediterranean thermohaline circulation and thus requires accu-
 699 rate estimation. We used the simulation results of a $1/8^\circ$
 700 resolution oceanic model that takes into account the pene-
 701 tration of the solar radiation with respect to depth. In order
 702 to respect the adequacy between the prognostic model
 703 MED8 and the diagnostic method, we applied a revised
 704 diagnosis, based on the Walin's method for the estimate of
 705 water mass transformation, that takes into account this
 706 vertical penetration of the solar radiation. This model was
 707 forced with ECMWF atmospheric fields, which allows a
 708 good representation of the oceanic circulation and of air-sea
 709 exchanges. We first compared the annual water mass
 710 transformation rate computed with the revised method with
 711 that obtained with the classical method. Major differences in
 712 estimates are observed, depending on the method applied,
 713 with a strong decrease in water mass transformation of
 714 about 40–50% in agreement with the global ocean analysis
 715 presented by *Iudicone et al.* [2007].

716 [43] This decrease results from the lower seasonal varia-
 717 tion when the penetrative solar radiation is considered. This
 718 can be explained by the fact that the solar radiation is then
 719 calculated over a wider density range, leading to weaker net
 720 values over a given density range. As well mixing that
 721 counterbalances production was previously overestimated in
 722 the annual budget. The greatest impact of the penetrative
 723 solar radiation occurs in spring and summer when the
 724 stratification of the water column is strong. Newly formed
 725 dense water is destroyed, at a rate of about 50% of the rate
 726 in winter.

727 [44] We computed water mass volume budgets during
 728 these two seasons. The two terms that are responsible for
 729 the volume variation are the transformation rate due to
 730 atmospheric fluxes (i.e., $F(\rho)$) and the interior mixing
 731 (i.e., diapycnal fluxes). The most striking change observed
 732 was for the densest water masses ($>27 \text{ kg/m}^3$) in summer.
 733 The penetrative solar radiation is therefore responsible for
 734 the destruction of these water masses, whereas, with the
 735 classical method, only mixing could play this role. In
 736 spring, mixing was previously underestimated for these
 737 densest waters. Regarding the light density range, mixing
 738 and transformation rate were previously overestimated both
 739 in spring and summer. We also show that about 1/3 of the

water mass transformation takes place below the surface 740
 layers. 741

[45] In this study, we give evidence of the crucial effect of 742
 taking into account the penetrative solar flux on water mass 743
 transformation diagnosis in the Mediterranean Sea. The next 744
 step for improving this effect would rely on a better 745
 parameterization of the penetration of the solar radiation 746
 in the prognostic model and in the diagnosis, possibly by 747
 including the variation in the absorption of the incoming 748
 solar radiation by the phytoplanktonic organisms in the 749
 water column which modulates the transparency of the 750
 seawater in space and time. The importance of this variation 751
 in the Mediterranean was shown by *Bosc et al.* [2004] from 752
 satellite ocean color-sensor data. We are also aware that our 753
 conclusions are sensitive to the vertical discretization of the 754
 model. This point is very delicate to investigate and should 755
 need to run again the prognostic model with a refine vertical 756
 grid which is beyond the scope of the present paper. 757

[46] **Acknowledgments.** We would like to thank K. Béranger, L. Li 758
 and G. Madec for fruitful discussions. We acknowledge financial support 759
 from the French national program GICC (Gestion et Impact du Changement 760
 Climatique) and the French Mercator project (www.mercator-ocean.fr). 761
 ECMWF analyses were kindly made available by the European Centre 762
 for Medium-range Weather Forecasts. Numerical simulations were per- 763
 formed on the NEC SX-5 of the Institut du Développement et des 764
 Ressources en Informatique Scientifique (IDRIS) of the Centre National 765
 de la Recherche Scientifique (CNRS). We thank Ray C. Griffiths for editing 766
 this manuscript. 767

References 768

- Alhammoud, B., K. Béranger, L. Mortier, M. Crépon, and I. Dekeyser 769
 (2005), Surface circulation of the Levantine Basin: Comparison of 770
 models results with observations, *Prog. Oceanogr.*, *66*, 299–320. 771
 Artegiani, A., D. Bregant, E. Paschini, N. Pinardi, F. Raicich, and A. Russo 772
 (1997), The Adriatic Sea general circulation. Part I: Air-sea interactions 773
 and water mass structure, *J. Phys. Oceanogr.*, *27*, 1492–1514. 774
 Astraldi, M., G. P. Gasparini, A. Vetrano, and S. Vignudelli (2002), Hydro- 775
 graphic characteristics and interannual variability of water masses in the 776
 central Mediterranean: A sensitivity test for long-term changes in the 777
 Mediterranean Sea, *Deep Sea Res., Part I*, *49*, 661–680. 778
 Barnier, B., L. Siefrid, and P. Marchesiello (1995), Thermal forcing for a 779
 global ocean circulation model using a three-year climatology of 780
 ECMWF analyses, *J. Mar. Syst.*, *6*, 363–380. 781
 Béranger, K., L. Mortier, L. Gervasio, G. P. Gasparini, M. Astraldi, and 782
 M. Crépon (2004), The surface circulation dynamics of the Sicily Strait: 783
 A comprehensive study from the observations to the models, the role of 784
 the topography, *Deep Sea Res., Part II*, *51*, 411–440. 785
 Béthoux, J. P. (1979), Budgets of the Mediterranean Sea. Their dependence 786
 on the local climate and on the characteristics of the Atlantic waters, 787
Oceanol. Acta, *2*, 157–163. 788
 Blanke, B., and P. Delecluse (1993), Variability of the tropical Atlantic 789
 Ocean simulated by a general circulation model with two different mixed 790
 layer physics, *J. Phys. Oceanogr.*, *23*, 1363–1388. 791
 Bosc, E., A. Bricaud, and D. Antoine (2004), Seasonal and interannual 792
 variability in algal biomass and primary production in the Mediterra- 793
 nean Sea, as derived from 4 years of SeaWiFS observations, *Global* 794
Biogeochem. Cycles, *18*, GB1005, doi:10.1029/2003GB002034. 795
 Drillet, Y., K. Béranger, M. Brémond, F. Gaillard, C. Le Provost, and 796
 S. Theetten (2000), Expérimentation PAM, in *Tech. Rep. MERCATOR* 797
Proj., Toulouse. 798
 Frouin, R., and S. F. Iacobellis (2002), Influence of phytoplankton 799
 on the global radiation budget, *J. Geophys. Res.*, *107*(D19), 4377, 800
 doi:10.1029/2001JD000562. 801
 Fuda, J. L., C. Millot, I. Taupier-Letage, U. Send, and J. M. Bocognano 802
 (2000), XBT monitoring of a meridian section across the western 803
 Mediterranean Sea, *Deep Sea Res., Part I*, *47*, 2191–2218. 804
 Garrett, C., R. Outerbridge, and K. Thompson (1993), Interannual varia- 805
 bility in Mediterranean heat and buoyancy fluxes, *J. Clim.*, *6*, 900–910. 806
 Gertman, I. F., I. M. Ovchinnikov, and Yu. I. Popov (1994), Deep con- 807
 vection in the eastern basin of the Mediterranean Sea, *Oceanology*, *34*, 808
 19–24. 809

- 810 Horton, C., J. Kerling, G. Athey, J. Schmitz, and M. Clifford (1994),
811 Airborne expendable bathythermograph surveys of the eastern Mediter-
812 ranean, *J. Geophys. Res.*, *99*, 9891–9905.
- 813 Iudicone, D., G. Madec, and T. J. McDougall (2007), Diagnosing water
814 transformations in neutral density space and the key role of light pen-
815 tration in the ocean, *J. Phys. Oceanogr.*, in press.
- 816 Jerlov, N. G. (1968), *Optical Oceanography*, 194 pp., Elsevier, New York.
- 817 Lacombe, H., and P. Tchernia (1972), Caractères hydrologiques et circula-
818 tion des eaux en Méditerranée, in *Mediterranean Sea*, edited by D. J.
819 Stanley, pp. 25–36, Hutchinson and Ross, Strasburg.
- 820 Large, W. G., and A. J. G. Nurser (2001), Ocean surface water mass trans-
821 formation, in *Ocean Circulation and Climate*, pp. 317–336, Academic
822 Press, New York.
- 823 Lascaratos, A., W. Roether, K. Nittis, and B. Klein (1999), Recent changes
824 in deep water formation and spreading in the eastern Mediterranean Sea:
825 A review, *Prog. Oceanogr.*, *44*, 5–36.
- 826 Lévy, M., A. Estublier, and G. Madec (2001), Choice of an advection
827 scheme for biogeochemical models, *Geophys. Res. Lett.*, *28*, 3725–3728.
- 828 Lewis, M. R., M.-E. Carr, G. C. Feldman, W. Esaias, and C. McClain
829 (1990), Influence of the penetrating solar radiation on the heat budget
830 of the equatorial Pacific Ocean, *Nature*, *347*, 543–545.
- 831 MacDonald, A., J. Candela, and H. L. Bryden (1994), An estimate of the
832 net heat transport through the Strait of Gibraltar, *Coastal Estuarine Stud.*,
833 vol. 46, AGU, Washington, D. C.
- 834 Madec, G., F. Lott, P. Delecluse, and M. Crépon (1996), Large-scale pre-
835 conditioning of deep-water formation in the northwestern Mediterranean
836 Sea, *J. Phys. Oceanogr.*, *26*, 1393–1408.
- 837 Madec, G., P. Delecluse, M. Imbard, and C. Lévy (1998), OPA8.1, in
838 *Ocean General Circulation Model, Reference Manual*, 97 pp., Note du
839 Pôle de modélisation de l'IPSL, Paris.
- 840 Marshall, J. C., A. J. G. Nurser, and R. G. Williams (1993), Inferring the
841 subduction rate and period over the North Atlantic, *J. Phys. Oceanogr.*,
842 *23*, 1315–1329.
- 843 MEDAR/MEDATLAS Group (2002), *MEDAR/MEDATLAS 2002 Data-*
844 *base. Cruise inventory, observed and analysed data of temperature and*
845 *bio-chemical parameters* [CD-ROM], MEDAR/MEDATLAS Group.
- 846 MEDOC Group (1970), Observation of formation of deep water in the
847 Mediterranean Sea, *Nature*, *227*, 1037–1040.
- 848 Mertens, C., and F. Schott (1998), Interannual variability of deep-water
849 formation in the northwestern Mediterranean, *J. Phys. Oceanogr.*, *28*,
850 1410–1424.
- 851 Millot, C. (1999), Circulation in the western Mediterranean Sea, *J. Mar.*
852 *Syst.*, *20*, 423–442.
- 853 Morel, A., and D. Antoine (1994), Heating rate within the upper ocean in
854 relation to its bio-optical state, *J. Phys. Oceanogr.*, *24*, 1652–1665.
- 855 Murtugudde, R., J. Beauchamp, C. R. McClain, M. Lewis, and A. J.
856 Busalacchi (2002), Effects of penetrative radiation on the upper tropical
857 ocean circulation, *J. Clim.*, *15*, 470–486.
- 858 Nurser, A. J. G., R. Marsh, and R. G. Williams (1999), Diagnosing water
859 mass formation from air-sea fluxes and surface mixing, *J. Phys. Oceanogr.*,
860 *29*, 1468–1487.
- Pacanowski, R. C., and A. Gnanadesikan (1998), Transient response in a
861 Z-level ocean model that resolve topography with partial cells, *Mon.*
862 *Weather Rev.*, *126*, 3248–3270. 863
- Poulain, P.-M. (2001), Adriatic Sea surface circulation as derived from
864 drifter data between 1990 and 1999, *J. Mar. Syst.*, *29*, 3–32. 865
- Reynolds, R. W. (1988), A real-time global sea surface temperature analy-
866 sis, *J. Clim.*, *1*, 75–86. 867
- Robinson, A. R., J. Sellschopp, A. Warn-Varnas, W. G. Leslie, C. J.
868 Lozano, P. J. Haley Jr., L. A. Anderson, and P. F. J. Lermusiaux
869 (1999), The atlantic ionian stream, *J. Mar. Syst.*, *20*, 129–156. 870
- Roether, W., and R. Schlitzer (1991), Eastern Mediterranean deep water
871 renewal on the basis of chlorofluoromethanes and tritium, *Dyn. Atmos.*
872 *Oceans*, *15*, 333–354. 873
- Roether, W., B. Klein, V. Beitzel, and B. B. Manca (1998), Property dis-
874 tributions and transient tracer ages in levantine intermediate water in the
875 eastern Mediterranean, *J. Mar. Syst.*, *18*, 71–87. 876
- Schott, F. A., and K. D. Leaman (1991), Hydrographic structure of the
877 convection regime in the Gulf of Lions: Winter 1987, *J. Phys. Oceanogr.*,
878 *21*, 575–598. 879
- Siefridt, L., Y. Drillet, R. Bourdalle-Badie, K. Béranger, C. Talatier, and
880 E. Greiner (2002), *Mise en Oeuvre du Modèle Mercator: Haute Résolution*
881 *sur l'Atlantique Nord et la Méditerranée*, Newsletter MERCATOR. 882
- Theocharis, A., B. Klein, K. Nittis, and W. Roether (2002), Evolution of
883 the eastern Mediterranean transient (1997–1999), *J. Mar. Syst.*, *33–34*,
884 91–116. 885
- Tziperman, E. (1986), On the role of interior mixing and air-sea fluxes in
886 determining the stratification and circulation of the oceans, *J. Phys.*
887 *Oceanogr.*, *16*, 680–693. 888
- Tziperman, E., and K. Speer (1994), A study of water mass transformation
889 in the Mediterranean Sea: Analysis of climatological data and a simple
890 three-box model, *Dyn. Atmos. Oceans*, *21*, 53–82. 891
- Vargas-Yañez, M., F. Plaza, J. Garcia-Lafuente, T. Sarhan, J. M. Vargas, and
892 P. Velez-Belchi (2000), About the seasonal variability of the Alboran Sea
893 circulation, *J. Mar. Syst.*, *35*, 229–248. 894
- Vilibic, I., and M. Orlic (2002), Adriatic water masses, their rates of for-
895 mation and transport through the Otranto Strait, *Deep Sea Res., Part I*,
896 *49*, 1321–1340. 897
- Walin, G. (1982), On the relation between sea-surface heat flow and the
898 thermal circulation in the ocean, *Tellus, Ser. A and Ser. B*, *34*, 187–195. 899
- Wust, G. (1961), On the vertical circulation of the Mediterranean Sea, 900
J. Geophys. Res., *66*, 3261–3271. 901
- P. Bouruet-Aubertot and M. Crépon, Laboratoire d'Océanographie et de 903
Climatologie - Expérimentation et Applications Numériques, LOCEAN/ 904
IPSL (previously LODYC), Paris, France. 905
- A. Bozec, COAPS, Florida State University, 222 Room Johnson 906
Building, 2035 E. Paul Dirac Drive, Tallahassee, FL 32310, USA. 907
(abozec@coaps.fsu.edu) 908
- D. Iudicone, Laboratory of Biological Oceanography, Stazione Zoologica, 909
SZN, Naples, Italy. 910

American Geophysical Union
Author Query Form

Journal: **Journal of Geophysical Research – Oceans**
Article Name: **Bozec (2007JC004606)**

Please answer all author queries.

1. Please provide complete mailing address of authors “P. Bouruet-Aubertot and M. Crépon” and “D. Iudicone”.
2. Please provide complete publisher's information for the following references.
 - *Drillet et al.*, 2000
 - *MacDonald et al.*, 1994
 - *MEDAR/MEDATLAS Group*, 2002
 - *Siefridt et al.*, 2002
3. Please provide an update for the publication status of the reference "*Iudicone et al.*, 2007, in press”.